Acta Physiol Scand 2005, 184, 187–193

Myocardial interstitial choline and glutamate levels during acute myocardial ischaemia and local ouabain administration

T. Kawada,[1] T. Yamazaki,[2] T. Akiyama,[2] T. Shishido,[1] H. Mori[2] and M. Sugimachi[1]

1 *Department of Cardiovascular Dynamics, National Cardiovascular Center Research Institute, Osaka, Japan*

2 *Department of Cardiac Physiology, National Cardiovascular Center Research Institute, Osaka, Japan*

Received 25 November 2004, accepted 16 March 2005
Correspondence: T. Kawada, Department of Cardiovascular Dynamics, National Cardiovascular Center Research Institute, 5-7-1 Fujishirodai, Suita, Osaka 565-8565, Japan.
E-mail: torukawa@res.ncvc.go.jp

Abstract

Aim: Noradrenaline (NA) uptake transporters are known to reverse their action during acute myocardial ischaemia and to contribute to ischaemia-induced myocardial interstitial NA release. By contrast, functional roles of choline and glutamate transporters during acute myocardial ischaemia remain to be investigated. Because both transporters are driven by the normal Na^+ gradient across the plasma membrane in a similar manner to NA transporters, the loss of Na^+ gradient would affect the transporter function, which would in turn alter myocardial interstitial choline and glutamate levels. The aim of the present study was to examine the effects of acute myocardial ischaemia and the inhibition of Na^+,K^+-ATPase on myocardial interstitial glutamate and choline levels.

Methods: In anaesthetized cats, we measured myocardial interstitial glutamate and choline levels while inducing acute myocardial ischaemia or inhibiting Na^+,K^+-ATPase by local administration of ouabain.

Results: The choline level was not changed significantly by ischaemia (from 0.93 ± 0.06 to 0.82 ± 0.13 μM, mean $\pm$ SE, $n = 6$) and was decreased slightly by ouabain (from 1.30 ± 0.06 to 1.05 ± 0.07 μM, $P < 0.05$, $n = 6$). The glutamate level was significantly increased from 9.5 ± 1.9 to 34.7 ± 6.1 μM by ischaemia ($P < 0.01$, $n = 6$) and from 8.9 ± 1.0 to 15.9 ± 2.3 μM by ouabain ($P < 0.05$, $n = 6$). Inhibition of glutamate transport by *trans*-L-pyrrolidine-2,4-dicarboxylate (*t*-PDC) suppressed ischaemia- and ouabain-induced glutamate release.

Conclusion: Myocardial interstitial choline level was not increased by acute myocardial ischaemia or by Na^+,K^+-ATPase inhibition. By contrast, myocardial interstitial glutamate level was increased by both interventions. The glutamate transporter contributed to glutamate release via retrograde transport.

Keywords acetylcholine, cardiac microdialysis, cats, coronary artery occlusion, myocardium, noradrenaline.

Acute myocardial ischaemia causes oxygen depletion and loss of ATP in the ischaemic region (Hearse 1979). Blockade of H^+-ATPase leads to noradrenaline (NA) leakage from storage vesicles and axoplasmic NA accumulation (Schömig *et al.* 1988). Intracellular acidosis causes Na^+ influx via Na^+/H^+ exchange. Inhibition of Na^+,K^+-ATPase activity reduces the Na^+ gradient across the plasma membrane. Because NA uptake transporters are driven by the normal Na^+ electrochemical gradient across the plasma membrane,

axoplasmic NA accumulation and reduction of the Na^+ gradient cause reverse transport of NA from the intracellular space to the extracellular space (Schwartz 2000). Acute myocardial ischaemia evokes the myocardial interstitial NA release in the ischaemic region via retrograde NA transport, independently of efferent sympathetic nerve activity (Schömig *et al.* 1984, Yamazaki *et al.* 1996, Akiyama & Yamazaki 1999, Kawada *et al.* 2001a).

Similar to NA, choline and glutamate are taken up into cells by plasma membrane transporters driven by the Na^+ gradient (Schwartz 2000). We hypothesized that the loss of Na^+ gradient under ischaemic conditions would interfere with the transporter function, which would in turn alter myocardial interstitial choline and glutamate levels. Choline release has been suggested as an index of ischaemic degradation of the myocardial phospholipid bilayer in isolated, Tyrode solution-perfused rat hearts (Brühl *et al.* 2004). Glutamate can be a preferred myocardial fuel during ischaemia and may have protective effects on ischaemic myocardium (Arsenian 1998). Measuring myocardial interstitial levels of these molecules *in vivo* would contribute to understanding the pathophysiology of acute myocardial ischaemia. To test the hypothesis, we employed an *in vivo* cardiac microdialysis technique and measured myocardial interstitial choline and glutamate levels in anaesthetized cats (Akiyama *et al.* 1991, 1994, Yamazaki *et al.* 1997, Kawada *et al.* 2001b). Acute myocardial ischaemia inevitably affects systemic haemodynamics and perfusion of the heart. To minimize such haemodynamic effects, we also examined the effects of Na^+,K^+-ATPase inhibition on the myocardial interstitial choline and glutamate levels by locally administering ouabain through a dialysis probe (Yamazaki *et al.* 1999, Kawada *et al.* 2002). The results of the present study indicated that the myocardial interstitial choline level was not increased by acute myocardial ischaemia or by Na^+,K^+-ATPase inhibition. By contrast, the myocardial interstitial glutamate level was increased by both interventions. The glutamate transporter contributed to glutamate release via retrograde transport.

Materials and methods

Surgical preparation

Animal care was conducted in strict accordance with the *Guiding Principles for the Care and Use of Animals in the Field of Physiological Sciences* approved by the Physiological Society of Japan. Adult cats weighing 2.0–4.8 kg were anaesthetized via an intraperitoneal injection of pentobarbital sodium (30–35 mg kg^{-1}) and ventilated mechanically with room air mixed with oxygen. The depth of anaesthesia was maintained with a continuous intravenous infusion of pentobarbital sodium (1–2 mg kg^{-1} h^{-1}) through a catheter inserted via the right femoral vein. Mean systemic arterial pressure was monitored from a catheter inserted via the right femoral artery.

With the animal in the lateral position, the left fifth and sixth ribs were resected to expose the heart. When a coronary occlusion was necessary, a 3-0 silk suture was prepared around the left anterior descending coronary artery (LAD) just distal to the first diagonal branch. With a fine guiding needle, a dialysis probe was implanted into the left ventricular free wall perfused by the LAD. Heparin sodium (100 U kg^{-1} bolus injection followed by a maintenance dose of 50 U kg^{-1} h^{-1}) was administered intravenously to prevent blood coagulation. At the end of the experiment the experimental animals were killed by an overdose of pentobarbital sodium. We confirmed that the dialysis probe had been implanted within the left ventricular myocardium.

Dialysis technique

We designed a transverse dialysis probe (Akiyama *et al.* 1991, 1994). For measurements of small molecular compounds including ACh, choline, and glutamate, we used a dialysis fibre of 50 000 molecular weight cutoff (13 mm length, 310 μm OD, 200 μm ID; PAN-1200, Asahi Chemical, Osaka, Japan) with both ends glued to polyethylene tubes (20 cm length, 500 μm OD, 200 μm ID). The dialysis probe was perfused at a rate of 2 μL min^{-1} with Ringer solution. Each sample was collected in a microtube containing 3 μL of phosphate buffer (100 mM, pH 3.5). A cholinesterase inhibitor eserine (100 μM) was added to the perfusate to measure ACh. A preliminary examination indicated that whether the perfusate-contained eserine did not affect myocardial interstitial choline levels significantly. Dead space volume between the dialysis fibre and the sample microtube was identical for ACh, choline, and glutamate measurements, and the sampling was performed taking into account the time for dialysate to traverse the dead space volume.

The dialysate ACh and choline levels were measured directly by high-performance liquid chromatography with electrochemical detection. The absolute detection limits of ACh and choline, determined with a signal-to-noise ratio of 3, were 10 and 5 fmol per injection, respectively. The dialysate glutamate level was measured by kinetic enzymatic analysis with CMA 600. The absolute detection limit of glutamate was 1 μM per injection.

Protocols

All protocols were started from 2 h after implanting the dialysis probe. To examine changes in myocardial

interstitial ACh and choline levels during acute myocardial ischaemia ($n = 6$), after collecting a 15-min baseline dialysate sample, we occluded the LAD for 60 min and obtained four consecutive 15-min dialysate samples. The full-length of the implanted dialysis fibre was located within the ischaemic area judged by discolouration of myocardium during the LAD occlusion. We then released the occlusion and collected a 15-min dialysate sample during reperfusion. To examine changes in myocardial ACh and choline levels in response to local ouabain administration ($n = 6$), after collecting a 15-min baseline dialysate sample, we replaced the perfusate with Ringer solution containing 100 μM ouabain and collected four consecutive 15-min dialysate samples.

In different groups of animals, myocardial interstitial glutamate levels were measured during acute myocardial ischaemia ($n = 6$) and during local administration of ouabain ($n = 6$). To elucidate the role of the glutamate transporter, we also examined the effects of glutamate transport inhibition by *trans*-L-pyrrolidine-2,4-dicarboxylate (*t*-PDC, 10 mM) on myocardial interstitial glutamate levels during acute myocardial ischaemia ($n = 7$) and local administration of ouabain ($n = 7$). *t*-PDC was locally administered through the dialysis probe to avoid systemic effects.

Statistical analysis

All data are presented as mean ± SE values. In each protocol, the effects of myocardial ischaemia or local ouabain administration were examined using one-way analysis of variance followed by Dunnett's test against the corresponding baseline level (Glantz 2002). The baseline as well as maximum glutamate levels with and without glutamate transport inhibition were compared by an unpaired *t*-test during acute myocardial ischaemia or during local ouabain administration (Glantz 2002). Differences were considered to be significant when $P < 0.05$.

Results

Figure 1a shows myocardial interstitial ACh level during acute myocardial ischaemia. The ACh level was increased by LAD occlusion, becoming approximately 15 times higher than the baseline level at 30–45 and 45–60 min of ischaemia. The ACh level decreased towards the baseline level upon reperfusion. Figure 1b illustrates myocardial interstitial choline level during acute myocardial ischaemia. The choline level did not change significantly throughout the ischaemic and reperfusion periods.

Figure 2a shows changes in myocardial interstitial ACh level during local administration of ouabain. The ACh level was increased by the inhibition of

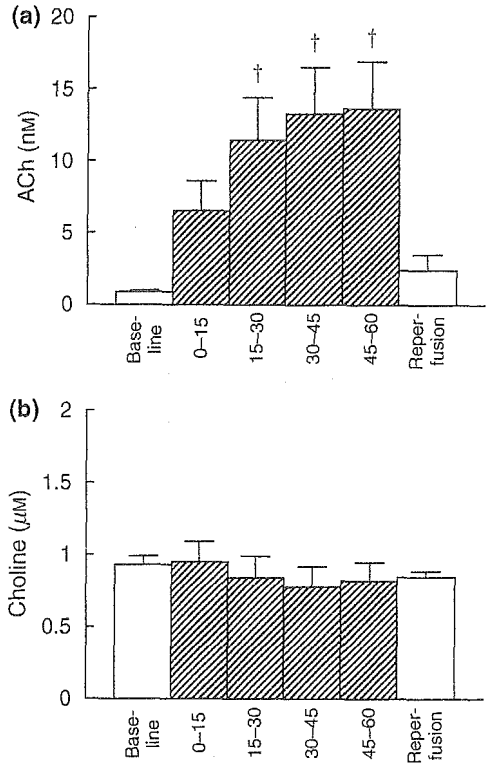

Figure 1 Changes in myocardial interstitial acetylcholine (ACh) level (a) and choline level (b) during coronary artery occlusion and reperfusion. Myocardial interstitial ACh level was significantly increased by acute myocardial ischaemia, while myocardial interstitial choline level was not changed. Data are mean ± SE. †$P < 0.01$ from baseline.

Na^+,K^+-ATPase, becoming approximately nine times higher than the baseline level at 15–30 min. The ACh level then decreased but remained significantly higher than the baseline level. Figure 2b illustrates the myocardial interstitial choline level during local administration of ouabain. The choline level was significantly lower at 0–15 and 45–60 min when compared with the baseline level.

Figure 3a shows changes in myocardial interstitial glutamate level during acute myocardial ischaemia. LAD occlusion increased the glutamate level to approximately 3.5 times higher than the baseline level at 0–15 min. Thereafter, the glutamate level was significantly higher than the baseline level throughout the ischaemic and reperfusion periods. Figure 3b illustrates the effects of glutamate transport inhibition on the ischaemia-induced glutamate release. The baseline glutamate level was significantly decreased by glutamate transport inhibition ($P < 0.05$). Although acute myocardial ischaemia and reperfusion significantly increased the glutamate level relative to the baseline level, the maximum glutamate level was attenuated to approximately one-fifth compared with that observed without glutamate transport inhibition ($P < 0.05$).

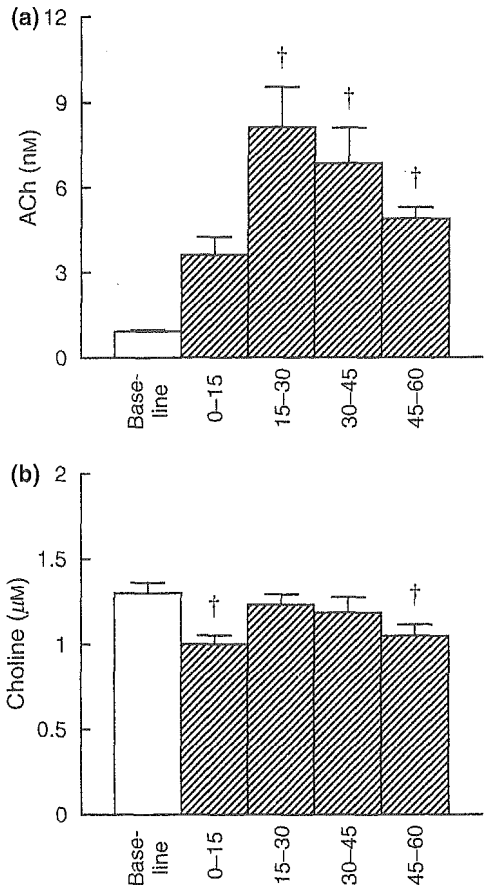

Figure 2 Changes in myocardial interstitial acetylcholine (ACh) level (a) and choline level (b) in response to the local administration of ouabain. Myocardial interstitial ACh level was significantly increased by ouabain. In contrast, myocardial interstitial choline level was decreased by ouabain. Data are mean ± SE. †$P < 0.01$ from baseline.

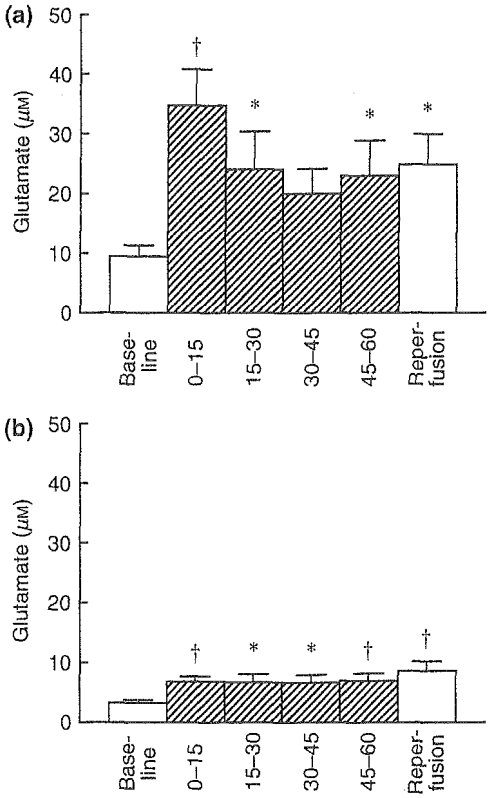

Figure 3 Changes in myocardial interstitial glutamate level during coronary artery occlusion and reperfusion without (a) and with (b) the inhibition of glutamate transporter. The glutamate level was significantly increased by acute myocardial ischaemia. The ischaemia-induced glutamate release was suppressed by the inhibition of glutamate transporter. Data are mean ± SE. †$P < 0.01$ and *$P < 0.05$ from baseline.

Figure 4a shows changes in myocardial interstitial glutamate level during the local administration of ouabain. Ouabain administration did not change the glutamate level at 0–15 min but increased the glutamate level thereafter. The glutamate level became approximately 1.8 times higher than the baseline level at 30–45 min. Figure 4b illustrates the effects of glutamate transport inhibition on ouabain-induced glutamate release. The baseline glutamate level was significantly decreased by the inhibition of glutamate transport ($P < 0.05$). Although ouabain administration increased the glutamate level relative to the baseline level, the maximum glutamate level was suppressed to approximately one-third of that observed without glutamate transport inhibition ($P < 0.05$).

Discussion

We have shown that acute myocardial ischaemia and local inhibition of Na^+,K^+-ATPase increased myocardial interstitial glutamate level but not choline level. Despite the similar Na^+ gradient dependency of corresponding transporters, myocardial interstitial glutamate and choline levels showed differential responses to the two interventions.

Changes in myocardial interstitial choline level

In the vagal nerve endings, ACh is hydrolysed to acetate and choline by acetylcholinesterase (Nicholls 1994). Choline is then taken up into the vagal nerve endings by the choline transporter driven by the Na^+ gradient. We hypothesized that loss of Na^+ gradient during acute myocardial ischaemia or local ouabain administration would increase the myocardial interstitial choline level by the interruption of choline uptake. Contrary to our hypothesis, acute myocardial ischaemia did not change myocardial interstitial choline level in the ischaemic region (Fig. 1b). Ouabain administration decreased the myocardial interstitial choline level at 0–15 and 45–60 min (Fig. 2b).

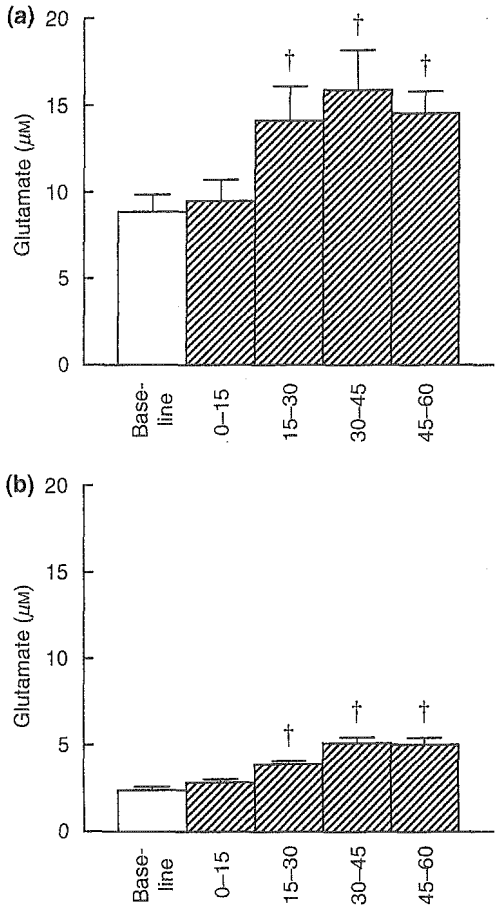

Figure 4 Changes in myocardial interstitial glutamate level in response to the local administration of ouabain without (a) and with (b) the inhibition of glutamate transporter. The glutamate level was significantly increased by ouabain administration. The ouabain-induced glutamate release was suppressed by the inhibition of glutamate transporter. Data are mean ± SE. †$P < 0.01$ from baseline.

Possible explanations for the absence of ischaemia- or ouabain-induced choline release are as follows. First, choline uptake is the rate-limiting step for ACh synthesis (Lockman & Allen 2002). Because choline in the intracellular space is rapidly consumed for ACh synthesis, the axoplasmic choline concentration might have been too low to evoke reverse transport by the choline transporter. Second, plasma choline concentration is stabilized by *de novo* choline synthesis from the catabolism of phosphatidylcholine found in cell membranes (Lockman & Allen 2002). Potential choline release may have been counterbalanced by the local stabilization mechanisms. Taking into account the recovery rate of the dialysis probe (approximately 30%), the myocardial interstitial choline concentration was 3–5 μM. Although the estimated concentration was lower than the highly regulated plasma choline concentration of approximately 10 μM, it was much higher than the ischaemia-induced maximum choline release (approximately 0.6 μM) in isolated rat hearts reported by Brühl *et al.* (2004). The present results suggest that myocardial interstitial choline level may not serve as an indicator of myocardial ischaemia in blood-perfused *in vivo* feline hearts.

By contrast with myocardial interstitial choline level, myocardial interstitial ACh level was increased both by acute myocardial ischaemia and by local administration of ouabain. Because ischaemia-induced ACh release was observed after vagal nerve transection in a previous study (Kawada *et al.* 2000), a Ca^{2+} channel-independent, regional release mechanism appears to be involved. Several reports have suggested that ouabain or ischaemia-induced intracellular Na^+ accumulation could elevate intracellular Ca^{2+} level via Na^+/Ca^{2+} exchange (Mochizuki & Jiang 1998, Li *et al.* 2000). The elevation of intracellular Ca^{2+} level may be associated with ACh release. Our previous study indicated that intracellular Ca^{2+} overload due to Ca^{2+} mobilization is responsible for the ACh release evoked by ischaemia (Kawada *et al.* 2000).

Changes in myocardial interstitial glutamate levels

Although the glutamate transporter family differs from the NA transporter family in that it requires counter-transport of K^+ instead of cotransport of Cl^-, its primary driving force is the Na^+ gradient across the plasma membrane (Schwartz 2000). Therefore, interventions that reduce the Na^+ gradient are likely to cause reverse transport of glutamate, in a similar manner to the reverse transport of NA. Acute myocardial ischaemia increased the myocardial interstitial glutamate level (Fig. 3a) as consistent with previous reports (Kennergren *et al.* 1997, 1999, Bäckström *et al.* 2003, Song *et al.* 1996). Inhibition of Na^+,K^+-ATPase also induced myocardial interstitial glutamate release (Fig. 4a). Glutamate release during acute myocardial ischaemia and local ouabain administration was significantly attenuated by the inhibition of glutamate transport (Figs 3b and 4b), suggesting the involvement of reverse transport by the glutamate transporter. Glutamate plays a vital role in keeping nitrogen balance in cells as a common amino acid in transamination reactions. The high intra-to-extracellular concentration ratio of glutamate would contribute to the retrograde transport by the glutamate transporter during the loss of normal Na^+ gradient.

In the case of myocardial interstitial NA levels, local blockade of NA uptake increased baseline NA levels, suggesting the accumulation of NA spontaneously released into the synaptic cleft (Akiyama & Yamazaki 1999). We therefore predicted that the inhibition of glutamate transport would increase the baseline gluta-

mate level. However, the inhibition of glutamate transport actually decreased the baseline glutamate level (Figs 3 and 4), suggesting that spontaneous glutamate release rather than glutamate uptake had occurred under baseline conditions. The insertion of a dialysis probe inevitably damages the myocardium. Although we waited for 2 h after implantation of the dialysis probe and the glutamate level declined with time, glutamate release from damaged myocardium may have continued. Notwithstanding this limitation, we were able to detect glutamate release in response to acute myocardial ischaemia and inhibition of Na^+,K^+-ATPase. Therefore, our interpretation that glutamate release was dependent on the reverse transport of glutamate transporter may be reasonable.

Supplementing the heart with glutamate has been shown to have beneficial effect on the recovery of contractile function in post-surgical patients (Arsenian 1998). The myocardial interstitial glutamate level remained increased during 15-min reperfusion whereas the myocardial interstitial ACh level returned towards the baseline level. Although the reason for different responses upon reperfusion was unanswered in the present study, the sustained increase in the glutamate level may have therapeutic effect on its own.

In conclusion, acute myocardial ischaemia and inhibition of Na^+,K^+-ATPase did not increase myocardial interstitial choline level despite a significant increase in myocardial interstitial ACh level. By contrast, both interventions significantly increased the myocardial interstitial glutamate level. The glutamate transporter contributed to myocardial interstitial glutamate release via retrograde transport.

This study was supported by Health and Labour Sciences Research Grant for Research on Advanced Medical Technology (H14-Nano-002) from the Ministry of Health Labour and Welfare of Japan, by Grant-in-Aid for Scientific Research (C-15590786) from the Ministry of Education, Science, Sports and Culture of Japan, and by the Program for Promotion of Fundamental Studies in Health Science of the Organization for Pharmaceutical Safety and Research from Pharmaceuticals and Medical Devices Agency (PMDA).

References

Akiyama, T. & Yamazaki, T. 1999. Norepinephrine release from cardiac sympathetic nerve endings in the in vivo ischemic region. *J Cardiovasc Pharmacol* 34(Suppl. 4), S11–S14.

Akiyama, T., Yamazaki, T. & Ninomiya, I. 1991. In vivo monitoring of myocardial interstitial norepinephrine by dialysis technique. *Am J Physiol Heart Circ Physiol* 261, H1643–H1647.

Akiyama, T., Yamazaki, T. & Ninomiya, I. 1994. In vivo detection of endogenous acetylcholine release in cat ventricles. *Am J Physiol Heart Circ Physiol* 266, H854–H860.

Arsenian, M. 1998. Potential cardiovascular applications of glutamate, aspartate, and other amino acids. *Clin Cardiol* 21, 620–624.

Bäckström, T., Goiny, M., Lockowandt, U., Liska, J. & Franco-Cereceda, A. 2003. Cardiac outflow of amino acids and purines during myocardial ischemia and reperfusion. *J Appl Physiol* 94, 1122–1128.

Brühl, A., Hafner, G. & Löffelholz, K. 2004. Release of choline in the isolated heart, an indicator of ischemic phospholipid degradation and its protection by ischemic preconditioning: no evidence for a role of phospholipase D. *Life Sci* 75, 1609–1620.

Glantz, S.A. 2002. *Primer of Biostatistics*, 5th edn. McGraw-Hill, New York.

Hearse, D.J. 1979. Oxygen deprivation and early myocardial contractile failure: a reassessment of the possible role of adenosine triphosphate. *Am J Cardiol* 44, 1115–1121.

Kawada, T., Yamazaki, T., Akiyama, T. *et al.* 2000. Differential acetylcholine release mechanisms in the ischemic and non-ischemic myocardium. *J Mol Cell Cardiol* 32, 405–414.

Kawada, T., Yamazaki, T., Akiyama, T. *et al.* 2001a. Vagosympathetic interactions in ischemia-induced myocardial norepinephrine and acetylcholine release. *Am J Physiol Heart Circ Physiol* 280, H216–H221.

Kawada, T., Yamazaki, T., Akiyama, T. *et al.* 2001b. In vivo assessment of acetylcholine-releasing function at cardiac vagal nerve terminals. *Am J Physiol Heart Circ Physiol* 281, H139–H145.

Kawada, T., Yamazaki, T., Akiyama, T. *et al.* 2002. Disruption of vagal efferent axon and nerve terminal function in the postischemic myocardium. *Am J Physiol Heart Circ Physiol* 283, H2687–H2691.

Kennergren, C., Nyström, B., Nyström, U. *et al.* 1997. In situ detection of myocardial infarction in pig by measurements of aspartate aminotransferase (ASAT) activity in the interstitial fluid. *Scand Cardiovasc J* 31, 343–349.

Kennergren, C., Mantovani, V., Lönnroth, P., Nyström, B., Berglin, E. & Hamberger, A. 1999. Extracellular amino acids as markers of myocardial ischemia during cardioplegic heart arrest. *Cardiology* 91, 31–40.

Li, S., Jiang, Q., Stys, P.K. 2000. Important role of reverse Na^+-Ca^{2+} exchange in spinal cord white matter injury at physiological temperature. *J Neurophysiol* 84, 1116–1119.

Lockman, P.R. & Allen, D.D. 2002. The transport of choline. *Drug Dev Ind Pharm* 28, 749–771.

Mochizuki, S. & Jiang, C. 1998. Na^+/Ca^{++} exchanger and myocardial ischemia/reperfusion. *Jpn Heart J* 39, 707–714.

Nicholls, D.G. 1994. *Proteins, Transmitters and Synapses*, pp. 186–199. Blackwell Science, London.

Schömig, A., Dart, A.M., Dietz, R., Mayer, E. & Kübler, W. 1984. Release of endogenous catecholamines in the ischemic myocardium of the rat. Part A: Locally mediated release. *Circ Res* 55, 689–701.

Schömig, A., Kurz, T., Richardt, G. & Schömig, E. 1988. Neuronal sodium homeostasis and axoplasmic amine concentration determine calcium-independent noradrenaline release in normoxic and ischemic rat heart. *Circ Res* 63, 214–226.

Schwartz, J.H. 2000. Neurotransmitters. In: E.R. Kandel, J.H. Schwartz & T.M. Jessell (eds) *Principles of Neural Science*, 4th edn, pp. 280–297. McGraw-Hill, New York.

Song, D., O'Regan, M.H. & Phillis, J.W. 1996. Release of the excitotoxic amino acids, glutamate and aspartate, from the isolated ischemic/anoxic rat heart. *Neurosci Lett* 220, 1–4.

Yamazaki, T., Akiyama, T., Kitagawa, H., Takauchi, Y. & Kawada, T. 1996. Elevation of either axoplasmic norepinephrine or sodium level induced release of norepinephrine from cardiac sympathetic nerve terminals. *Brain Res* 737, 343–346.

Yamazaki, T., Akiyama, T., Kitagawa, H., Takauchi, Y., Kawada, T. & Sunagawa, K. 1997. A new, concise dialysis approach to assessment of cardiac sympathetic nerve terminal abnormalities. *Am J Physiol Heart Circ Physiol* 272, H1182–H1187.

Yamazaki, T., Akiyama, T. & Kawada, T. 1999. Effects of ouabain on in situ cardiac sympathetic nerve endings. *Neurochem Int* 35, 439–445.

Am J Physiol Heart Circ Physiol 289: H301–H307, 2005.
First published February 11, 2005; doi:10.1152/ajpheart.01237.2004.

Prediction of circulatory equilibrium in response to changes in stressed blood volume

Kazunori Uemura,[1] Toru Kawada,[1] Atsunori Kamiya,[1] Takeshi Aiba,[1,2] Ichiro Hidaka,[1,3] Kenji Sunagawa,[4] and Masaru Sugimachi[1]

[1]*Department of Cardiovascular Dynamics, National Cardiovascular Center Research Institute, Suita;* [2]*Pharmaceuticals and Medical Devices Agency, Tokyo;* [3]*Japan Association for the Advancement of Medical Equipment, Tokyo; and* [4]*Department of Cardiovascular Medicine, Kyushu University Graduate School of Medical Science, Fukuoka, Japan*

Submitted 7 December 2004; accepted in final form 4 February 2005

Uemura, Kazunori, Toru Kawada, Atsunori Kamiya, Takeshi Aiba, Ichiro Hidaka, Kenji Sunagawa, and Masaru Sugimachi. Prediction of circulatory equilibrium in response to changes in stressed blood volume. *Am J Physiol Heart Circ Physiol* 289: H301–H307, 2005. First published February 11, 2005; doi:10.1152/ajpheart.01237.2004.—Accurate prediction of cardiac output (CO), left atrial pressure (P_{LA}), and right atrial pressure (P_{RA}) is a prerequisite for management of patients with compromised hemodynamics. In our previous study (Uemura et al. *Am J Physiol Heart Circ Physiol* 286: H2376–H2385, 2004), we demonstrated a circulatory equilibrium framework, which permits the prediction of CO, P_{LA}, and P_{RA} once the venous return surface and integrated CO curve are known. Inasmuch as we also showed that the surface can be estimated from single-point CO, P_{LA}, and P_{RA} measurements, we hypothesized that a similar single-point estimation of the CO curve would enable us to predict hemodynamics. In seven dogs, we measured the P_{LA}-CO and P_{RA}-CO relations and derived a standardized CO curve using the logarithmic function $CO = S_L[\ln(P_{LA} - 2.03) + 0.80]$ for the left heart and $CO = S_R[\ln(P_{RA} - 2.13) + 1.90]$ for the right heart, where S_L and S_R represent the preload sensitivity of CO, i.e., pumping ability, of the left and right heart, respectively. To estimate the integrated CO curve in each animal, we calculated S_L and S_R from single-point CO, P_{LA}, and P_{RA} measurements. Estimated and measured CO agreed reasonably well. In another eight dogs, we altered stressed blood volume (−8 to +8 ml/kg of reference volume) under normal and heart failure conditions and predicted the hemodynamics by intersecting the surface and the CO curve thus estimated. We could predict CO [$y = 0.93x + 6.5$, $r^2 = 0.96$, standard error of estimate (SEE) = 7.5 ml·min^{-1}·kg^{-1}], P_{LA} ($y = 0.90x + 0.5$, $r^2 = 0.93$, SEE = 1.4 mmHg), and P_{RA} ($y = 0.87x + 0.4$, $r^2 = 0.91$, SEE = 0.4 mmHg) reasonably well. In conclusion, single-point estimation of the integrated CO curve enables accurate prediction of hemodynamics in response to extensive changes in stressed blood volume.

logarithmic function; venous return surface; heart failure

ACCURATE PREDICTION of cardiac output (CO) and cardiac filling pressures after therapeutic interventions is indispensable for optimal management and improved prognosis of patients with compromised hemodynamics (4, 5, 13, 23). In the 1980s, Sunagawa's group (20, 27) extended the framework of circulatory equilibrium of Guyton and co-workers (9, 10) to analyze complicated hemodynamic conditions such as left-sided heart failure. The extended framework is composed of a venous return surface representing the venous return of the systemic and pulmonary circulations and an integrated CO curve representing the pumping ability of the left and the right heart (Fig. 1) (27). The intersection point of the venous return surface and the integrated cardiac curve gives the equilibrium CO, left atrial pressure (P_{LA}), and right atrial pressure (P_{RA}). Changes in stressed blood volume shift the venous return surface upward or downward, altering the equilibrium point accordingly.

Our previous study (29) experimentally validated that venous return is a linear function of P_{LA} and P_{RA} and that this relation is expressed by a flat surface, i.e., the venous return surface (Fig. 1). In addition, because of the small intra- and interanimal variability in the slope of the surface, only a single set of CO, P_{LA}, and P_{RA} values is sufficient to estimate the venous return surface. Furthermore, it is possible to predict how the venous return surface shifts in response to a known amount of change in the stressed blood volume. These findings suggest that if the integrated CO curve can be estimated from a single set of CO, P_{LA}, and P_{RA} values, it is possible to predict hemodynamics in response to various therapeutic interventions, which induce changes in loading condition or in the pumping ability of the heart (29). The present study was therefore undertaken to develop a method to estimate the integrated CO curve from a single set of CO, P_{LA}, and P_{RA} values and to examine whether intersection of the integrated CO curve and the venous return surface thus estimated predicts hemodynamics in response to extensive changes in the stressed blood volume. Using our model, we were able to estimate the CO curve and predict the hemodynamics in anesthetized, open-chest dogs under conditions of left heart failure as well as normal cardiac function.

METHODS

Integrated CO Curve

In our previous study, we showed that CO is closely related to P_{LA} or P_{RA} by a three-parameter logarithmic function (29)

$$CO = S_L \times [\ln (P_{LA} - F_L) + H_L] \quad (1)$$

$$CO = S_R \times [\ln (P_{RA} - F_R) + H_R] \quad (2)$$

where S_L, F_L, and H_L and S_R, F_R, and H_R are parameters.

To estimate the integrated CO curve from a single set of CO, P_{LA}, and P_{RA} values, we fixed the F and H parameters according to the following rationale. It is well known that the CO curve varies widely with changes in ventricular contractility, heart rate, vascular resistance, and diastolic stiffness (8, 10, 20, 21, 24, 30). As shown in the APPENDIX, these factors are mainly included in the S parameter rather than in the F or H parameters. The S parameter thus comprehensively

Address for reprint requests and other correspondence: K. Uemura, Dept. of Cardiovascular Dynamics, National Cardiovascular Center Research Institute, 5-7-1 Fujishirodai, Suita 565-8565, Japan (E-mail: kuemura@ri.ncvc.go.jp).

The costs of publication of this article were defrayed in part by the payment of page charges. The article must therefore be hereby marked "*advertisement*" in accordance with 18 U.S.C. Section 1734 solely to indicate this fact.

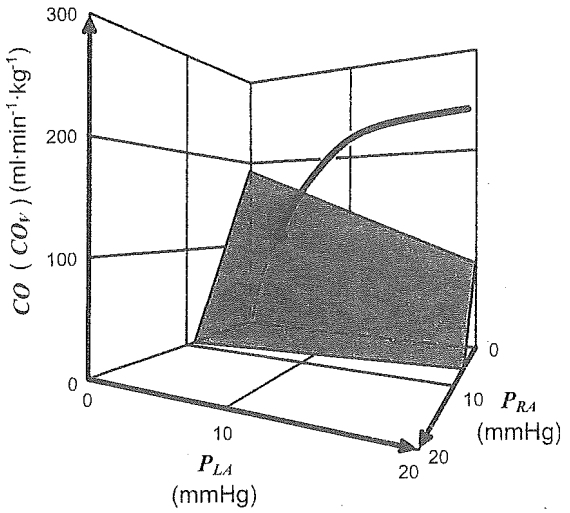

Fig. 1. Diagram of circulatory equilibrium for cardiac output (CO), venous return (CO_V), left atrial pressure (P_{LA}), and right atrial pressure (P_{RA}). Equilibrium CO, P_{LA}, and P_{RA} are obtained as the intersection point of the venous return surface and the integrated CO curve. [Modified from Uemura et al. (29).]

represents the pumping ability of the left or right heart. Therefore, we hypothesized that variations in the CO curve can be explained exclusively by the *S* parameter. Once standard values of the *F* and *H* parameters are determined, we can estimate the integrated CO curve by calculating the *S* parameter from a single set of CO, P_{LA}, and P_{RA} values.

Animal Preparation

We used 15 adult mongrel dogs of either gender (20–30 kg body wt). Care of the animals was in strict accordance with the "Guiding Principles for the Care and Use of Animals in the Field of Physiological Sciences" approved by the Physiological Society of Japan. Anesthesia was induced with pentobarbital sodium (25 mg/kg), and endotracheal intubation was performed. Isoflurane (1.5%) was continuously inhaled to maintain an appropriate level of anesthesia during the experiment. Catheters (6-Fr) were placed in the right femoral artery and vein for withdrawal of blood and for administration of drugs and fluids. To stabilize autonomic tone, we isolated the carotid sinuses bilaterally and maintained the intrasinus pressure constant at 120 mmHg (22). The cervical vagosympathetic trunks were cut. Systemic arterial pressure was measured by a catheter-tipped micromanometer (model PC-751, Millar Instruments, Houston, TX) placed in the ascending aorta via the right carotid artery. After a median sternotomy, a small pericardial incision was made at the level of the aortic root. An ultrasonic flowmeter (model 20A594, Transonics, Ithaca, NY) was placed around the ascending aorta via the incision to measure CO. Fluid-filled catheters were placed in the left and right atria via the incision to measure P_{LA} and P_{RA}, respectively. They were connected to pressure transducers (model DX-200, Nihon Kohden, Tokyo, Japan). The junction between the inferior vena cava and the right atrium was taken as the reference point for zero pressure (22).

Experimental Protocol

Under normal control conditions, we first infused ~250 ml of 10% dextran solution via the right femoral vein. We withdrew blood from the femoral artery in steps of 2 ml/kg to a total volume of 16–22 ml/kg (8–11 steps per animal). In each step, after waiting for 1 min, we recorded CO, P_{LA}, and P_{RA} for ~10 s (Fig. 2). We assumed that this volume reduction alters only the stressed blood volume of the systemic and pulmonary circulation. Because we isolated the baroreceptors, baroreflex-related changes in unstressed blood volume were negligible. We defined the reference values of CO, P_{LA}, and P_{RA} when half of the volume reduction was attained.

To create left ventricular failure, we embolized the left circumflex coronary artery with 90-μm-diameter glass microspheres (28). We adjusted the number of microspheres injected so as to increase P_{LA} by 20 mmHg. We then volume loaded the animals and repeated the protocol described above.

The data were recorded while respiration was temporarily suspended at end expiration. All analog signals were digitized at 200 Hz with a 12-bit analog-to-digital converter (model AD12-16UE, Contec, Osaka, Japan) using a dedicated laboratory computer system (model MA 20V, NEC, Tokyo, Japan) and were stored on a hard disk for subsequent analysis. All the recorded data were averaged over 5 s. All data, except pressure data, were normalized to individual body weight.

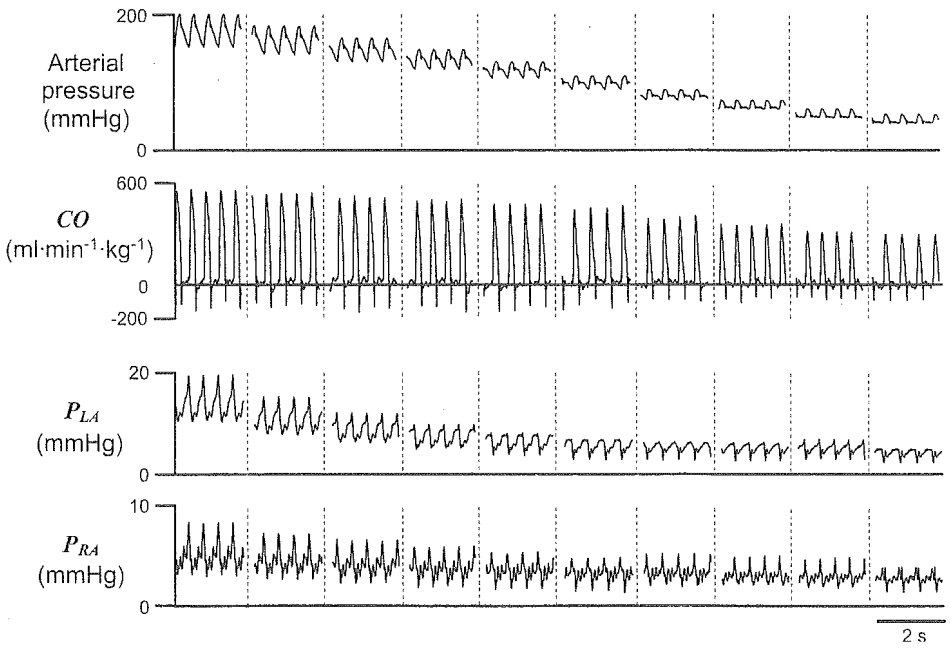

Fig. 2. Changes in arterial pressure, CO, P_{LA}, and P_{RA} throughout the examination. As P_{RA} and P_{LA} decrease after stepwise reduction of the stressed blood volume, CO also decreases (Frank-Starling mechanism).

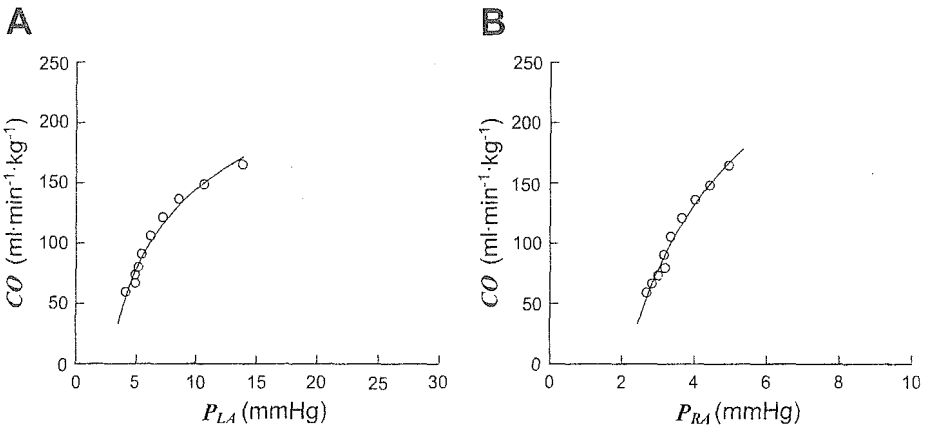

Fig. 3. Relation between CO and P_{LA} (*A*) and between CO and P_{RA} (*B*) in 1 dog. Solid curves, best fit of the 3-parameter logarithmic functions obtained by least-squares method.

Data Analysis

Determination of standard values of F and H parameters. We determined the standard values of the *F* and *H* parameters in seven randomly selected dogs (*group 1*). Using the least-squares method, we fitted the P_{LA}-CO and P_{RA}-CO relations obtained under normal conditions to the three-parameter logarithmic functions (*Eqs. 1* and *2*). We averaged the *F* and *H* values of the left and right heart for the seven animals. The averaged values were used as the standard *F* and *H* parameters in subsequent analyses.

Estimation of the integrated CO curve. Using the standard *F* and *H* parameters, we examined whether we could estimate the integrated CO curve from a single set of CO, P_{LA}, and P_{RA} values. For each animal in *group 1*, we calculated the *S* parameter by substituting the reference values of CO, P_{LA}, and P_{RA} into *Eqs. 1* and *2*. This calculation was done under normal and heart failure conditions. After calculation of the *S* parameter, the P_{LA} and P_{RA} measured in each step were substituted into *Eq. 1* to estimate CO of the left heart and into *Eq. 2* to estimate CO of the right heart. The estimated and measured CO were compared by linear regression analyses.

Prediction of circulatory equilibrium. In the other eight dogs (*group 2*), we estimated the integrated CO curve and venous return surface. The CO curve was estimated as described above using the standard *F* and *H* parameters. Venous return surface was estimated according to our previous work (29) as follows

$$CO_V = V/0.129 - 19.61P_{RA} - 3.49P_{LA} \quad (3)$$

where V is the stressed blood volume, CO_V is the integrated venous return, and 0.129 (min), 19.61 ($ml \cdot min^{-1} \cdot kg^{-1} \cdot mmHg^{-1}$), and 3.49 ($ml \cdot min^{-1} \cdot kg^{-1} \cdot mmHg^{-1}$) are standard parameters characterizing the venous return surface (29). The reference CO, P_{LA}, and P_{RA} values were used to calculate V, which served as the reference stressed volume.

With altered V (from +8 to −8 ml/kg of the reference value), we numerically determined the intersection of the venous return surface (*Eq. 3*) and the integrated CO curve (*Eqs. 1* and *2*) to predict CO, P_{LA}, and P_{RA}. The predicted CO, P_{LA}, and P_{RA} were compared with the measured values. We considered the change in V (±8 ml/kg) to be substantial relative to the physiological stressed blood volume (~25 ml/kg) (17).

Statistics

Group data are expressed as means (SD). The level of statistical significance was defined as $P < 0.05$. To test the goodness of fit, the coefficient of determination (r^2) and the standard error of estimate (SEE) were calculated.

RESULTS

Determination of the Standard Parameters

Figure 3 shows the measured P_{LA}-CO and P_{RA}-CO relations in a representative dog. CO increases in response to increases in P_{LA} or P_{RA} by the Frank-Starling mechanisms. These relations could be fitted to the three-parameter logarithmic function as follows: $CO = 66.7[\ln(P_{LA} - 2.08) + 0.1]$, $r^2 = 0.98$, SEE = 5.9 $ml \cdot min^{-1} \cdot kg^{-1}$ (Fig. 3*A*) and $CO = 112.7[\ln(P_{RA} - 1.39) + 0.19]$, $r^2 = 0.98$, SEE = 5.5 $ml \cdot min^{-1} \cdot kg^{-1}$ (Fig. 3*B*).

Table 1 summarizes the results of the fit in seven dogs. Coefficients of determination were high for the left heart (r^2 = 0.95–0.99) and the right heart (r^2 = 0.90–0.99). These results indicated that the logarithmic functions represented the CO curves of the left and right heart with good accuracy. The averaged *F* and *H* values (F_L = 2.03 mmHg, H_L = 0.80, F_R = 2.13 mmHg, and H_R = 1.90) for seven animals were used as standard values in subsequent analyses.

Table 1. *Fit of CO-P_{LA} and CO-P_{RA} relations to three-parameter logarithmic functions*

Dog	S_L	F_L	H_L	r^2	SEE
1	58.1	1.27	0.61	0.98	4.3
2	24.4	2.03	2.71	0.95	3.6
3	108.4	0.00	−0.67	0.95	5.6
4	66.7	2.08	0.08	0.98	5.9
5	105.6	2.30	−0.02	0.99	5.0
6	73.5	2.21	0.59	0.99	2.5
7	42.0	4.32	2.30	0.98	4.7
Mean (SD)	68.4 (30.9)	2.03 (1.29)	0.80 (1.25)	0.97	4.5 (1.2)
Dog	S_R	F_R	H_R	r^2	SEE
1	46.7	2.12	2.34	0.98	4.7
2	33.9	1.50	2.50	0.96	3.3
3	64.1	2.10	2.10	0.90	8.2
4	112.7	1.39	0.19	0.98	5.5
5	101.8	1.39	0.92	0.99	4.6
6	80.6	3.07	1.59	0.99	2.8
7	37.1	3.33	3.69	0.94	6.8
Mean (SD)	68.1 (31.3)	2.13 (0.8)	1.90 (1.14)	0.96	5.1 (1.9)

S_L and S_R ($ml \cdot min^{-1} \cdot kg^{-1}$), F_L and F_R (mmHg), and H_L and H_R (unitless), parameters of the logarithmic function for left and right hearts, respectively (see METHODS for calculations); r^2, coefficient of determination; SEE, standard error of the estimate ($ml \cdot min^{-1} \cdot kg^{-1}$).

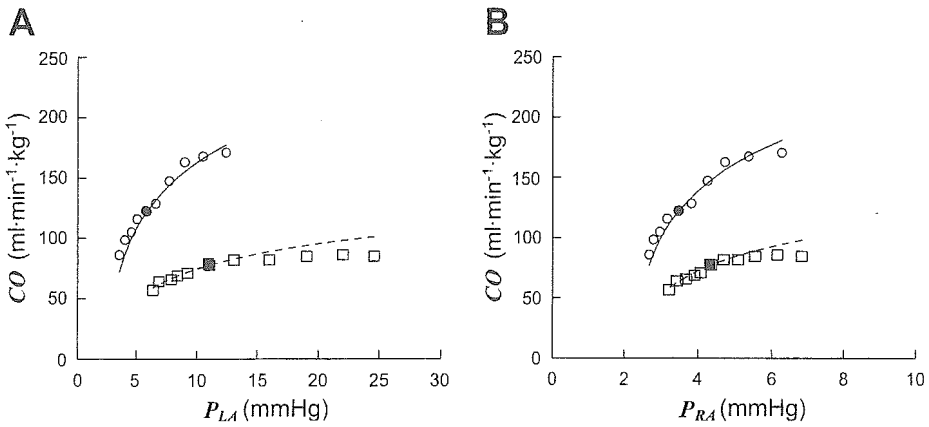

Fig. 4. CO curves for 1 animal under normal conditions and left ventricular failure for the left heart (*A*) and the right heart (*B*). ●, Reference hemodynamic values under normal conditions; ■, reference hemodynamic values under left ventricular failure; ○, measured points under normal conditions; □, measured points under left ventricular failure. Estimated CO curves under normal conditions (solid lines) and under left ventricular failure (dashed lines) accurately correspond with measured points.

Estimation of the Integrated CO Curve

Figure 4 shows the estimated CO curves under normal and heart failure conditions for a single animal. From the reference values, we calculated individual values of the *S* parameter. Under normal conditions, the estimated CO curve accurately coincided with the measured points in the left and the right heart. A good agreement was also observed under left ventricular failure.

Figure 5 demonstrates the relation between estimated and measured CO of pooled data from seven animals (*group 1*). The estimated CO agreed with the measured CO in the left and right heart.

Prediction of Circulatory Equilibrium

Figure 6 illustrates the accuracy of prediction of hemodynamics in response to changes in stressed blood volume (8 dogs, *group 2*). Figure 6*A* shows the relation between predicted and measured CO. CO was predicted accurately over a wide range of CO values from 30 to 200 ml·min^{-1}·kg^{-1}. A small intercept value with a slope near unity also indicates the accuracy of prediction. Figure 6*B* shows the accuracy of the P_{LA} prediction. Although variability increased in the high pressure range (>20 mmHg), the prediction was reasonably accurate. Similarly, P_{RA} was also predicted with reasonable accuracy (Fig. 6*C*).

DISCUSSION

The results of this study indicate that once a single set of steady-state CO, P_{LA}, and P_{RA} values is available, it is possible to predict the changes in hemodynamic variables resulting from a known amount of change in stressed blood volume. This prediction can be very helpful in management of patients under unstable hemodynamic conditions (13, 23).

Estimation of the Integrated CO Curve

We have shown that the integrated CO curve can be estimated with reasonable accuracy under normal and heart failure conditions (Figs. 4 and 5). By fixing the *F* and *H* parameters and by ascribing the changes in the CO curve exclusively to the *S* parameter, we were able to estimate the integrated CO curve from a single set of hemodynamic measurements. As shown in the APPENDIX, the *F* and *H* parameters are mainly related to the end-diastolic pressure-volume relation (*Eq. A4*). In advanced cardiac disorders seen clinically, the end-diastolic pressure-volume relation may vary drastically (6, 7). Hypertensive or idiopathic cardiomyopathy sometimes induces severe ventricular hypertrophy, thereby significantly altering the diastolic ventricular pressure-volume relation (14). In such cases, it may be desirable not to use fixed values but, rather, to estimate *F* and *H* parameters in individual patients. The cardiovascular properties shown in *Eq. A4* can be estimated noninvasively under a steady-state hemodynamic condition (3, 12). Integration of these properties into our method may allow independent estimation of the three parameters in individual patients.

The following validations indicate that our mathematical model of the CO curve and its estimation are consistent with previous investigations. First, on the basis of *Eq. A4* (see

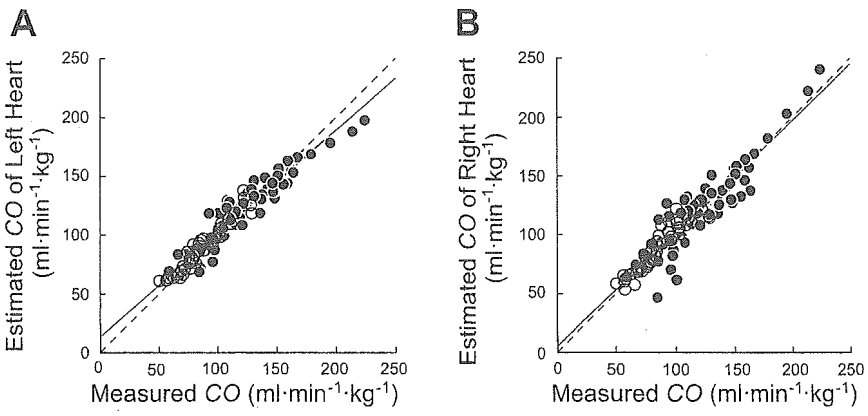

Fig. 5. Relation between estimated and measured values of CO for left heart (*A*) and right heart (*B*) for 104 steps pooled over 13 CO curves. ●, Normal cardiac function; ○, left heart failure; dashed line, line of identity. Regression analysis (solid line) reveals that estimated CO agrees well with measured CO in the left heart [y = 0.88x + 13.3, n = 104, r^2 = 0.93, standard error of estimate (SEE) = 8.7 ml·min^{-1}·kg^{-1}] and right heart (y = 0.96x + 5.0, n = 104, r^2 = 0.88, SEE = 12.1 ml·min^{-1}·kg^{-1}).

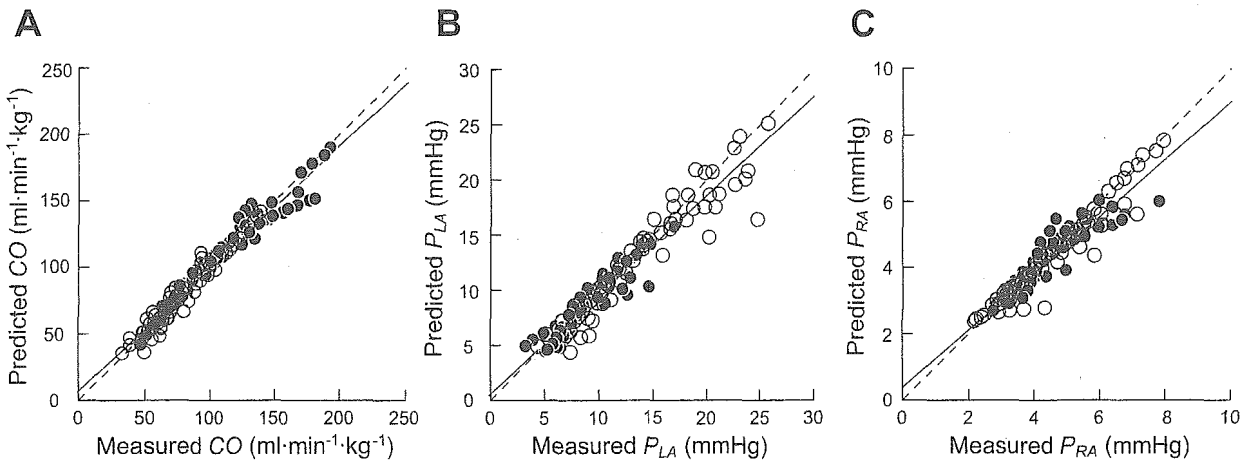

Fig. 6. Relation between predicted and measured values for CO (*A*), P_{LA} (*B*), and P_{RA} (*C*) for 128 steps under normal cardiac function (●) and left heart failure (○). Dashed line, line of identity. Prediction was done by intersecting the venous return surface and the integrated CO curve, both of which were estimated from a set of reference hemodynamic values. Regression analysis (solid line) reveals that predicted CO ($y = 0.93x + 6.5$, $n = 128$, $r^2 = 0.96$, SEE = 7.5 ml·min^{-1}·kg^{-1}), P_{LA} ($y = 0.90x + 0.5$, $n = 128$, $r^2 = 0.93$, SEE = 1.4 mmHg), and P_{RA} ($y = 0.87x + 0.4$, $n = 128$, $r^2 = 0.91$, SEE = 0.4 mmHg) agree reasonably well with measured values.

APPENDIX), using previously reported data (6, 11, 18, 25), we calculated the three parameters in the logarithmic function for the left heart. The values of the cardiovascular properties were chosen to be appropriate for a 20-kg dog (Table 2). The calculated S_L (34 ml·min^{-1}·kg^{-1}), F_L (3.2 mmHg), and H_L (1.14) were compatible with those obtained in our experiment (Table 1). Second, Pouleur et al. (19) examined the CO curve of the left heart in dogs under various cardiac conditions (control, coronary occlusion, and nitroprusside infusion under control and coronary occlusion). Their CO curves could be approximated to our three-parameter logarithmic functions with reasonable accuracy ($r^2 = 0.94$–0.99). When we applied the standard values of F_L (2.03 mmHg) and H_L (0.80) obtained in this study to their data and estimated their CO curve, the estimated CO closely correlated with the values measured ($y = 0.67x + 29.0$, $r^2 = 0.90$, SEE = 5.0 ml·min^{-1}·kg^{-1}, from 40 to 150 ml·min^{-1}·kg^{-1}).

Clinical Application of the Framework of Circulatory Equilibrium

Cardiac patients frequently receive empirical fluid challenges to treat low CO, unexplained hypotension, and oliguria (1, 32). Such empirical challenges sometimes exert deleterious effects by excessive volume expansion (1, 32). Our framework is free of such problems, because we can accurately estimate the stressed blood volume of the patient and predict hemodynamics resulting from the volume challenge, once we measure a single set of steady-state CO, P_{LA}, and P_{RA} values with, for example, Swan-Ganz catheters (2).

Table 2. *Values of the cardiovascular properties from previously reported data*

Parameter	Value
HR, beats/min	120
T, min	0.0083
R, mmHg·min·ml^{-1}	0.031
E_{es}, mmHg/ml	10
V_0, ml	5
k, ml^{-1}	0.13
α, mmHg	0.25
β, mmHg	4.8
γ (unitless)	1.5

HR, heart rate; T, heart period; R, systemic arterial resistance; E_{es}, end-systolic elastance of left ventricle; V_0, volume at which end-systolic pressure is 0 mmHg in the left ventricle; k, α, and β, constants characterizing end-diastolic pressure-volume relation of the left ventricle; γ, ratio of left ventricular end-diastolic pressure to mean left atrial pressure.

The outcome of acute or chronic heart failure has been related to the severity of reduced CO and elevated left ventricular filling pressure (4, 5, 13, 23). Several studies, however, indicate that patients with Forrester class IV hemodynamics are not necessarily condemned to a class IV prognosis. Even if the initial hemodynamics are classified as class IV, patients showing reduction in filling pressure after intensive medical therapy have a better prognosis than those without reduction in filling pressure (13, 23). With use of our framework for guidance, proper management of low CO and elevated filling pressures would improve the prognosis of such patients.

In clinical settings, the reference point for zero pressure is determined by an empirical external inspection (16). Changes in the patient's position relative to the pressure transducer may induce apparent changes in atrial pressures (16). These factors can result in a measurement error for atrial pressure and, consequently, an error in the prediction of the circulatory equilibrium. Accurate determination of the external reference point relative to the level of the right atrium and strict attention to patient position are required for clinical application of our framework.

Limitations of the Study

All the experiments of this study were conducted in anesthetized, open-chest dogs. Anesthesia and surgical trauma significantly affect the cardiovascular system (31). Whether this equilibrium framework can be applied to conscious, closed-chest animals (including humans) remains to be tested.

We isolated baroreceptors and fixed the autonomic tone in this study. This was necessary, because the baroreflex alters the CO curve and venous return surface through its effects on stressed blood volume, vascular resistance, heart rate, and cardiac contractility (8, 22). How changes in autonomic tone under the closed-loop condition affect the accuracy of hemodynamic prediction remains to be investigated.

Conclusion

The integrated CO curve can be estimated on the basis of a single set of hemodynamic measurements (CO, P_{LA}, and P_{RA}). The integrated CO curve thus estimated enables accurate prediction of hemodynamics (CO, P_{LA}, and P_{RA}) after extensive changes in stressed blood volume during heart failure and normal cardiac function.

APPENDIX

Mathematical modeling of the CO curve. We derived the relation between CO and atrial pressure on the basis of the ventricular pressure-volume relation framework (15, 25) and the ventricular-arterial coupling framework (26) as follows.

The relation between the stroke volume (SV) and the ventricular end-diastolic volume (V_{ed}) has been approximated with reasonable accuracy as

$$SV = \frac{TE_{es}}{TE_{es} + R} \times (V_{ed} - V_0) \qquad (A1)$$

where E_{es} is the slope (elastance), V_0 is the volume axis intercept of the ventricular end-systolic pressure-volume relation, T is the heart period, and R is the arterial resistance (20, 25, 26). Dividing SV by T, CO can be expressed as

$$CO = \frac{E_{es}}{TE_{es} + R} \times (V_{ed} - V_0) \qquad (A2)$$

V_{ed} can be interrelated with end-diastolic pressure (P_{ed}) by

$$P_{ed} = \alpha e^{kV_{ed}} + \beta \qquad (A3)$$

where k, α, and β are constants (6, 7). If we approximate P_{ed} by a scaled mean atrial pressure (P_{At}), γP_{At} (γ is a proportionality constant), *Eq. A2* can be rewritten as

$$CO = \frac{1}{k} \cdot \frac{E_{es}}{TE_{es} + R} \times \left[\ln \left(P_{At} - \frac{\beta}{\gamma} \right) + \ln \left(\frac{\gamma}{\alpha} \right) - kV_0 \right] \qquad (A4)$$

which can be simplified by lumping parameters for cardiovascular system properties into three constants, S, F, and H

$$CO = S \times [\ln (P_{At} - F) + H] \qquad (A5)$$

GRANTS

This study was supported by Health and Labor Sciences Research Grants for research on medical devices for analyzing, supporting, and substituting the function of the human body and research on advanced medical technology from the Ministry of Health, Labour, and Welfare of Japan, Japan Society for the Promotion of Science Grants-in-Aid for Scientific Research A 15200040, C 14570707, and C 15590786, and Ministry of Education, Culture, Sports, Science, and Technology Grant-in-Aid for Young Scientists (B) 16700379, as well as the Program for Promotion of Fundamental Studies in Health Science of Pharmaceuticals and Medical Devices Agency of Japan.

REFERENCES

1. **Bendjelid K, Suter PM, and Romand JA.** The respiratory change in preejection period: a new method to predict fluid responsiveness. *J Appl Physiol* 96: 337–342, 2004.
2. **Chaliki HP, Hurrell DG, Nishimura RA, Reinke RA, and Appleton CP.** Pulmonary venous pressure: relationship to pulmonary artery, pulmonary wedge, and left atrial pressure in normal, lightly sedated dogs. *Catheter Cardiovasc Interv* 56: 432–438, 2002.
3. **Chen CH, Fetics B, Nevo E, Rochitte CE, Chiou KR, Ding PA, Kawaguchi M, and Kass DA.** Noninvasive single-beat determination of left ventricular end-systolic elastance in humans. *J Am Coll Cardiol* 38: 2028–2034, 2001.
4. **Crexells C, Chatterjee K, Forrester JS, Dikshit K, and Swan HJ.** Optimal level of filling pressure in the left side of the heart in acute myocardial infarction. *N Engl J Med* 289: 1263–1266, 1973.
5. **Forrester JS, Diamond G, Chatterjee K, and Swan HJG.** Medical therapy of acute myocardial infarction by application of hemodynamic subsets. *N Engl J Med* 295: 1356–1362, 1976.
6. **Glantz SA and Kernoff RS.** Muscle stiffness determined from canine left ventricular pressure-volume curves. *Circ Res* 37: 787–794, 1975.
7. **Glantz SA and Parmley WW.** Factors which affect the diastolic pressure-volume curve. *Circ Res* 42: 171–180, 1978.
8. **Greene AS and Shoukas AA.** Changes in canine cardiac function and venous return curves by the carotid baroreflex. *Am J Physiol Heart Circ Physiol* 251: H288–H296, 1986.
9. **Guyton AC.** Determination of cardiac output by equating venous return curves with cardiac response curves. *Physiol Rev* 35: 123–129, 1955.
10. **Guyton AC, Jones CE, and Coleman TG.** *Circulatory Physiology: Cardiac Output and Its Regulation* (2nd ed.). Philadelphia, PA: Saunders, 1973, p. 263–284.
11. **Lee RW and Goldman S.** Mechanism for decrease in cardiac output with atrial natriuretic peptide in dogs. *Am J Physiol Heart Circ Physiol* 256: H760–H765, 1989.
12. **Little WC, Ohno M, Kitzman DW, Thomas JD, and Cheng CP.** Determination of left ventricular chamber stiffness from the time for deceleration of early left ventricular filling. *Circulation* 92: 1933–1939, 1995.
13. **Lucas C, Johnson W, Hamilton MA, Fonarow GC, Woo MA, Flavell CM, Creaser JA, and Stevenson LW.** Freedom from congestion predicts good survival despite previous class IV symptoms of heart failure. *Am Heart J* 140: 840–847, 2000.
14. **Mandinov L, Eberli FR, Seiler C, and Hess OM.** Diastolic heart failure. *Cardiovasc Res* 45: 813–825, 2000.
15. **Maughan WL, Shoukas AA, Sagawa K, and Weisfeldt ML.** Instantaneous pressure-volume relationship of the canine right ventricle. *Circ Res* 44: 309–315, 1979.
16. **McGee SR.** Physical examination of venous pressure: a critical review. *Am Heart J* 136: 10–18, 1998.
17. **Ogilvie RI and Zborowska-Sluis D.** Effect of chronic rapid ventricular pacing on total vascular capacitance. *Circulation* 85: 1524–1530, 1992.
18. **Ohno M, Cheng CP, and Little WC.** Mechanism of altered patterns of left ventricular filling during the development of congestive heart failure. *Circulation* 89: 2241–2250, 1994.
19. **Pouleur H, Covell JW, and Ross J Jr.** Effects of nitroprusside on venous return and central blood volume in the absence and presence of acute heart failure. *Circulation* 61: 328–337, 1980.
20. **Sagawa K, Maughan WL, Suga H, and Sunagawa K.** *Cardiac Contraction and Pressure-Volume Relationship.* Oxford, UK: Oxford Univ. Press, 1988, p. 232–298.
21. **Sarnoff SJ and Berglund E.** Ventricular function. 1. Starling's law of the heart, studied by means of simultaneous right and left ventricular function curves in the dog. *Circulation* 9: 706–718, 1953.
22. **Shoukas AA.** Carotid sinus baroreceptor reflex control and epinephrine. Influence on capacitive and resistive properties of the total pulmonary vascular bed of the dog. *Circ Res* 51: 95–101, 1982.
23. **Stevenson LW, Tillisch JH, Hamilton M, Luu M, Chelimsky-Fallick C, Moriguchi J, Kobashigawa J, and Walden J.** Importance of hemodynamic response to therapy in predicting survival with ejection fraction less than or equal to 20% secondary to ischemic or nonischemic dilated cardiomyopathy. *Am J Cardiol* 66: 1348–1354, 1990.
24. **Stone HL, Bishop VS, and Dong EJ.** Ventricular function in cardiac denervated and cardiac sympathectomized conscious dogs. *Circ Res* 20: 587–593, 1967.

25. **Suga H and Sagawa K.** Instantaneous pressure-volume relationships and their ratio in the excised, supported canine left ventricle. *Circ Res* 35: 117–126, 1974.
26. **Sunagawa K, Maughan WL, Burkhoff D, and Sagawa K.** Left ventricular interaction with arterial load studied in isolated canine ventricle. *Am J Physiol Heart Circ Physiol* 245: H773–H780, 1983.
27. **Sunagawa K, Sagawa K, and Maughan WL.** Ventricular interaction with the loading system. *Ann Biomed Eng* 12: 163–189, 1984.
28. **Todaka K, Leibowitz D, Homma S, Fisher PE, Derosa C, Stennett R, Packer M, and Burkhoff D.** Characterizing ventricular mechanics and energetics following repeated coronary microembolization. *Am J Physiol Heart Circ Physiol* 272: H186–H194, 1997.
29. **Uemura K, Sugimachi M, Kawada T, Kamiya A, Jin Y, Kashihara K, and Sunagawa K.** A novel framework of circulatory equilibrium. *Am J Physiol Heart Circ Physiol* 286: H2376–H2385, 2004.
30. **Ursino M.** Interaction between carotid baroregulation and the pulsating heart: a mathematical model. *Am J Physiol Heart Circ Physiol* 275: H1733–H1747, 1998.
31. **Vatner SF and Braunwald E.** Cardiovascular control mechanisms in the conscious state. *N Engl J Med* 293: 970–976, 1975.
32. **Wagner JG and Leatherman JW.** Right ventricular end-diastolic volume as a predictor of the hemodynamic response to a fluid challenge. *Chest* 113: 1048–1054, 1998.

Resetting of the arterial baroreflex increases orthostatic sympathetic activation and prevents postural hypotension in rabbits

Atsunori Kamiya[1], Toru Kawada[1], Kenta Yamamoto[1], Daisaku Michikami[1], Hideto Ariumi[1], Kazunori Uemura[1], Can Zheng[1], Syuji Shimizu[1], Takeshi Aiba[1], Tadayoshi Miyamoto[1], Masaru Sugimachi[1] and Kenji Sunagawa[2]

[1] *Department of Cardiovascular Dynamics, National Cardiovascular Centre Research Institute, Osaka, Japan*
[2] *Department of Cardiovascular Medicine, Kyusyu University Graduate School of Medical Sciences, Fukuoka, Japan*

Since humans are under ceaseless orthostatic stress, the mechanism to maintain arterial pressure (AP) under orthostatic stress against gravitational fluid shift is of great importance. We hypothesized that (1) orthostatic stress resets the arterial baroreflex control of sympathetic nerve activity (SNA) to a higher SNA, and (2) resetting of the arterial baroreflex contributes to preventing postural hypotension. Renal SNA and AP were recorded in eight anaesthetized, vagotomized and aortic-denervated rabbits. Isolated intracarotid sinus pressure (CSP) was increased stepwise from 40 to 160 mmHg with increments of 20 mmHg (60 s for each CSP level) while the animal was placed supine and at 60 deg upright tilt. Upright tilt shifted the CSP–SNA relationship (the baroreflex neural arc) to a higher SNA, shifted the SNA–AP relationship (the baroreflex peripheral arc) to a lower AP, and consequently moved the operating point to marked high SNA while maintaining AP. A simulation study suggests that resetting in the neural arc would double the orthostatic activation of SNA and increase the operating AP in upright tilt by 10 mmHg, compared with the absence of resetting. In addition, upright tilt did not change the CSP–AP relationship (the baroreflex total arc). A simulation study suggests that although a downward shift of the peripheral arc could shift the total arc downward, resetting in the neural arc would compensate this fall and prevent the total arc from shifting downward to a lower AP. In conclusion, upright tilt increases SNA by resetting the baroreflex neural arc. This resetting may compensate for the reduced pressor responses to SNA in the peripheral cardiovascular system and contribute to preventing postural hypotension.

(Resubmitted 10 March 2005; accepted after revision 29 April 2005; first published online 5 May 2005)
Corresponding author A. Kamiya: Department of Cardiovascular Dynamics, National Cardiovascular Centre Research Institute, Osaka 565-8565, Japan. Email: kamiya@ri.ncvc.go.jp

The maintenance of arterial pressure (AP) under orthostatic stress against gravitational fluid shift is of great importance, but the mechanisms remain unknown. During standing, a gravitational fluid shift directed toward the lower part of the body (such as the abdominal vascular bed and lower limbs) will cause severe postural hypotension if not counteracted by compensatory mechanisms (Rowell, 1993). Arterial baroreflexes have been considered to be the major compensatory mechanism (Persson & Kirchheim, 1991; Eckberg & Sleight, 1992; Rowell, 1993) since denervation of baroreceptor afferents causes profound postural hypotension (Sato *et al.* 2002). Earlier studies have characterized baroreflexes and their control of sympathetic nerve activity (SNA) and heart rate (Rea & Eckberg, 1987; Persson & Kirchheim, 1991; Eckberg & Sleight, 1992; Rudas *et al.* 1999; DiCarlo & Bishop, 2001; Kawada *et al.* 2003). However, the role of baroreflexes in orthostatic posture is little known. What determines AP and SNA in response to orthostatic stress remains unclear.

The baroreflex is a negative feedback control system functioning physiologically to attenuate perturbations in AP (Eckberg & Sleight, 1992; Sato *et al.* 1999). Baroreflex equilibrium diagram analysis is, to our knowledge, the best method to define the operating point (operating SNA and AP) of baroreflex (Sato *et al.* 1999). The equilibrium diagram consists of the neural and peripheral arcs. The neural arc represents the static input–output relationship between baroreceptor pressure and SNA, whereas the peripheral arc represents the relationship between SNA

DOI: 10.1113/jphysiol.2005.086512

and systemic AP. The intersection of the neural and peripheral arcs defines the operating point of AP regulation in the baroreflex closed-loop condition (for details, see Methods, Theoretical considerations: coupling of neural and peripheral arcs) (Sato *et al.* 1999; Yamamoto *et al.* 2004).

In contrast to supine posture, in orthostatic posture a gravitational body fluid shift directed toward the lower part of the body (Rowell, 1993) decreases the effective circulatory blood volume (Sagawa *et al.* 1988; Rowell, 1993). Therefore, orthostatic stress probably attenuates the pressor response to SNA in the cardiovascular system (i.e. the baroreflex peripheral arc). If orthostatic stress resets the baroreflex neural arc to augment SNA, the resetting would compensate for the attenuated pressor response of the baroreflex peripheral arc and prevent AP falling under orthostatic stress. We hypothesized that (1) orthostatic stress resets the baroreflex neural arc to a higher SNA, and (2) resetting of the arterial baroreflex contributes to preventing postural hypotension.

Methods

Theoretical considerations: coupling of neural and peripheral arcs (Fig. 1)

The arterial baroreflex is a negative feedback control system that senses AP (strictly, transmural pressure; Angell James, 1971) by baroreceptors and regulates it. When the baroreflex feedback loop is closed, baroreceptor input pressure (i.e. carotid sinus pressure; CSP) equals AP. This situation makes it difficult to analyse the behaviour of the arterial baroreflex. In this study, we used a baroreflex open-loop equilibrium diagram analysis. We opened the baroreflex loop by isolating the baroreceptor element from the systemic circulation, and changed the input baroreceptor pressure independently of systemic AP. Moreover, we measured the efferent SNA, and divided the baroreflex system into the neural arc (from baroreceptor pressure input to efferent SNA) and the peripheral arc (from SNA to AP) (Fig. 1*A*, middle panel). The neural arc is a reverse sigmoid relation and the peripheral arc is a sigmoid relation (Fig. 1*A*, top and bottom panels).

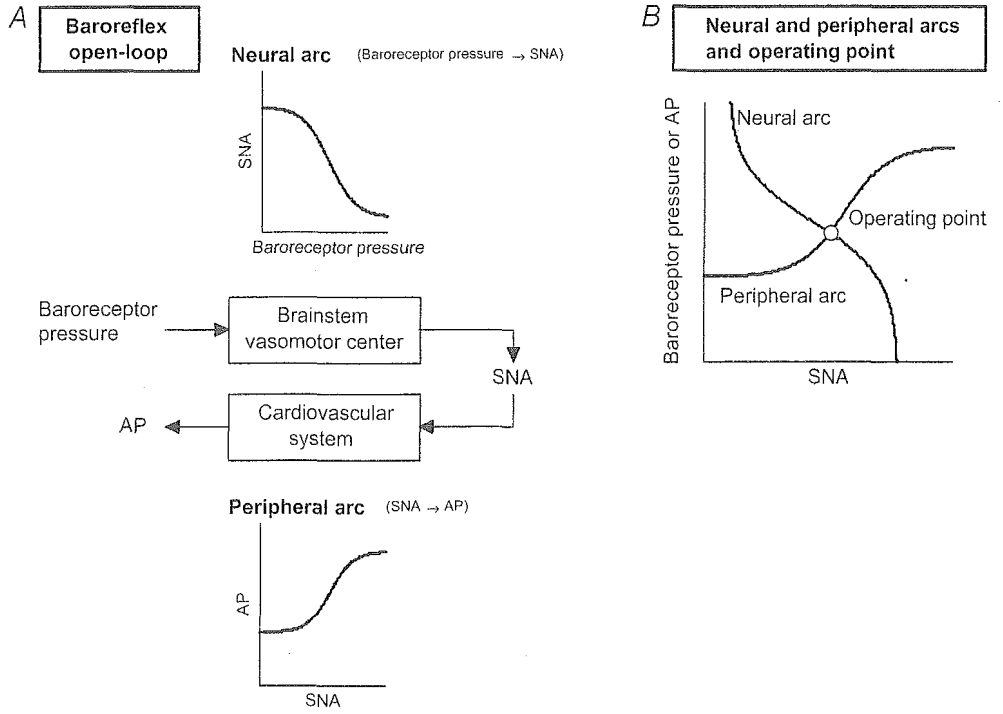

Figure 1. Theoretical considerations of the coupling of baroreflex neural and peripheral arcs
Although the baroreflex is a negative feedback control system that senses arterial pressure (AP) by baroreceptors and regulates AP, we opened the loop by changing baroreceptor pressure independently of AP (*A*). By measuring sympathetic nerve activity (SNA), we divided the baroreflex system into the neural arc (from baroreceptor pressure input to efferent SNA) and the peripheral arc (from SNA to AP) (*A*, middle panel). Both arcs show sigmoidal input–output relationships (*A*, top and bottom panels). Since baroreceptor pressure is equilibrated with AP under the baroreflex closed-loop condition, the intersection when these two arcs are superimposed defines the operating point of the baroreflex feedback system (*B*).

Importantly, baroreceptor pressure equals AP in the baroreflex closed-loop condition. Accordingly, when the two relationships are superimposed (Fig. 1*B*), the intersection of these arcs defines the operating point of the baroreflex feedback system. The validity of this framework has been confirmed in earlier studies showing that the AP and SNA estimated from the intersection agree with those measured in the closed-loop condition (Sato *et al.* 1999; Yamamoto *et al.* 2004).

Surgical preparations

Animals were cared for in strict accordance with the *Guiding Principles for the Care and Use of Animals in the Field of Physiological Science* of the Physiological Society of Japan. Eight Japanese White rabbits weighing 2.4–3.3 kg were initially anaesthetized by intravenous injection (2 ml kg^{-1}) of a mixture of urethane (250 mg ml^{-1}) and α-chloralose (40 mg ml^{-1}). Anaesthesia level were maintained by continuously infusing the anaesthetics at a rate of 0.33 ml kg^{-1} h^{-1} using a syringe pump (CFV-3200, Nihon Kohden, Tokyo). The rabbits were mechanically ventilated with oxygen-enriched room air. The bilateral carotid sinuses were isolated vascularly from systemic circulation by ligating the internal and external carotid arteries and other small branches originating from the carotid sinus regions. The isolated carotid sinuses were filled with warm physiological saline through catheters inserted via the common carotid arteries. The CSP was measured using a fluid-filled pressure transducer (AP-630G, Nihon Kohden, Tokyo) at the level of the carotid sinus throughout the experiment, and controlled by a servo-controlled piston pump (model ET-126 A; Labworks, Costa Mesa, CA, USA). In this condition, changes in carotid artery dimension are proportional to changes in carotid artery pressure. Bilateral vagal and aortic depressor nerves were sectioned at the middle of the neck to eliminate reflexes from the cardiopulmonary region and the aortic arch. Systemic AP was measured using a high-fidelity pressure transducer (Millar Instruments; Houston, TX, USA) inserted retrograde from the right common carotid artery below the isolated carotid sinus region. Body temperature was maintained at around 38°C with a heating pad. Additional injection of anaesthetics were never required as judged from haemodynamics (AP) in supine posture that were stable in the course of experiments.

We exposed the left renal sympathetic nerve retroperitoneally and attached a pair of stainless steel wire electrodes (Bioflex wire AS633; Cooner Wire, Chatworth, CA, USA) to record renal SNA. The nerve fibres peripheral to the electrodes were tightly ligated and crushed to eliminate afferent signals from the kidney. The nerve and electrodes were covered with a mixture of silicone gel (Silicon Low Viscosity, KWIK-SIL; World Precision Instrument, Inc., FL, USA) to insulate and immobilize the electrodes. The preamplified nerve signal was band-pass filtered at 150–1000 Hz, full-wave rectified and low-pass filtered with a cut-off frequency of 30 Hz to quantify the nerve activity. Pancuronium bromide (0.1 mg kg^{-1}) was administered to prevent contamination of muscular activity in the SNA recording. After all protocols were finished, animals were killed by intravenous infusion of hexamethonium bromide (6 mg kg^{-1}).

Protocols

After the surgical preparation, the animal was maintained in the supine position (0 deg) on a tilt bed. To stabilize the posture, the head was fixed full-frontal to the bed by strings, and the body and legs were rigged up in a clothes-like bag. In protocol 1, the static non-linear characteristics of the sympathetic baroreflex system were estimated in the supine position. CSP was decreased to 40 mmHg, and then increased stepwise from 40 to 160 mmHg with increments of 20 mmHg. Each CSP step was maintained for 60 s.

In protocol 2, to obtain the actual operating pressure in the baroreflex closed-loop condition in both supine and 60 deg upright positions, CSP was matched with systemic AP via the servo-controlled piston pump. The animal was kept supine for 10 min, and then tilted upright to 60 deg within 10 s by inclining the tilt bed to 60 deg and dropping the lower regions of rabbit with the fulcrum set at the level of the carotid sinus. The 60 deg upright posture was maintained for 10 min. Since the clothes-like bag stabilized the posture of the animals, there was no additional mechanical movement that reduced the quality of measurements. The position of the head remained almost fixed during the tilt to minimize vestibular stimulation.

In protocol 3, the static non-linear characteristics of the sympathetic baroreflex system were estimated during the 60 deg upright tilt. CSP was increased stepwise from 40 to 160 mmHg similar to protocol 1.

Data analysis

In protocols 1 and 3, AP and SNA were averaged during the last 10 s of each CSP level. For normalization of SNA, the noise level when animals were killed after experiments was assigned 0 arbitrary units (a.u). The mean SNA at CSP of 40 mmHg in the supine position were assigned 100 arbitrary units (a.u). Other SNA signals in both postures were normalized to these units.

The relationship between the input (CSP in the neural arc, SNA in the peripheral arc, CSP in the total arc) and

output (SNA in the neural arc, AP in the peripheral arc, AP in the total arc) is parametrically characterized by a four-parameter logistic equation model as follows (Kent *et al.* 1972):

$$y = \frac{P_1}{1 + \exp[P_2(x - P_3)]} + P_4 \quad (1)$$

where y is the output and x the input, P_1 is the response range of change in y, P_2 is the coefficient for calculating gain, P_3 is the value of x corresponding to the mid-point of operation, and P_4 is the minimum value of y. Instantaneous gain was calculated from the first derivative of the logistic function (the maximum gain equals $-P_1P_4/4$ at $x = P_3$). The intersection of the neural and peripheral arc curves on the equilibrium diagram was defined as the estimated operating point (Fig. 1), in supine and upright tilt positions. The hypothetical operating point during upright tilt (in which tilt changes the peripheral arc, but not the neural arc), was simulated by using the intersections of the supine neural arc and the upright tilt peripheral arc.

The measured operating AP and SNA of the baroreflex were obtained in protocol 2. AP and SNA were averaged during the last 3 min in the baroreflex closed-loop condition both in the supine position and with 60 deg upright tilt.

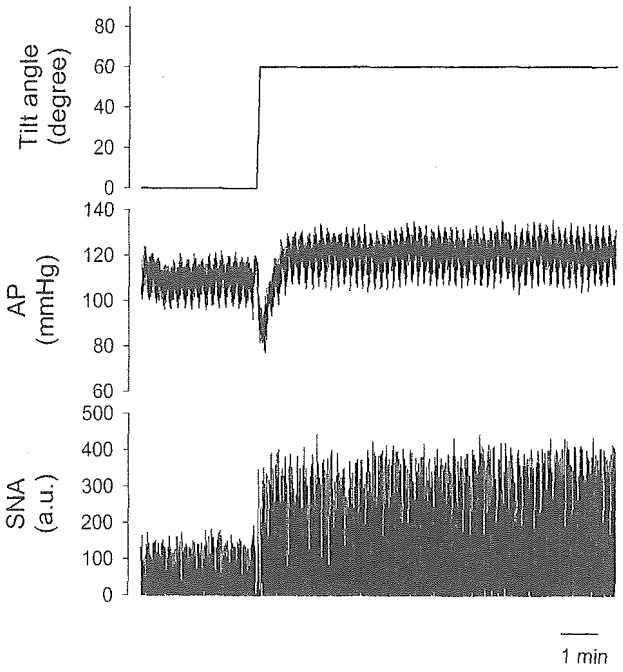

Figure 2. Time series of SNA and AP in response to a postural change from horizontal supine (3 min) to 60 deg upright tilt position (10 min)
Data were resampled at 10 Hz. The SNA and AP reach a steady state within 3 min.

Statistic analysis

All data are presented as means ± S.D. Student's paired t test was used to compare the parameters of the neural and peripheral arcs and operating points between postures (Glantz, 1997). Differences were considered significant when $P < 0.05$. A linear regression analysis was used to compare the operating points estimated from the equilibrium diagram with those measured (Glantz, 1997).

Results

Figures 2–4 show examples of data derived from the same animal. In the baroreflex closed-loop condition, 60 deg upright tilt rapidly decreased and then increased AP, and transiently decreased and then increased SNA (Fig. 2). Both AP and SNA reached nearly steady states within 3 min (Fig. 2).

In the baroreflex open-loop condition, SNA and AP decreased in response to stepwise increase in CSP both in the supine position (Fig. 3*A*) and at 60 deg upright tilt (Fig. 3*B*). In the neural arc, SNA was higher during upright tilt than supine at all CSP levels (Fig. 4*A*). The upright tilt

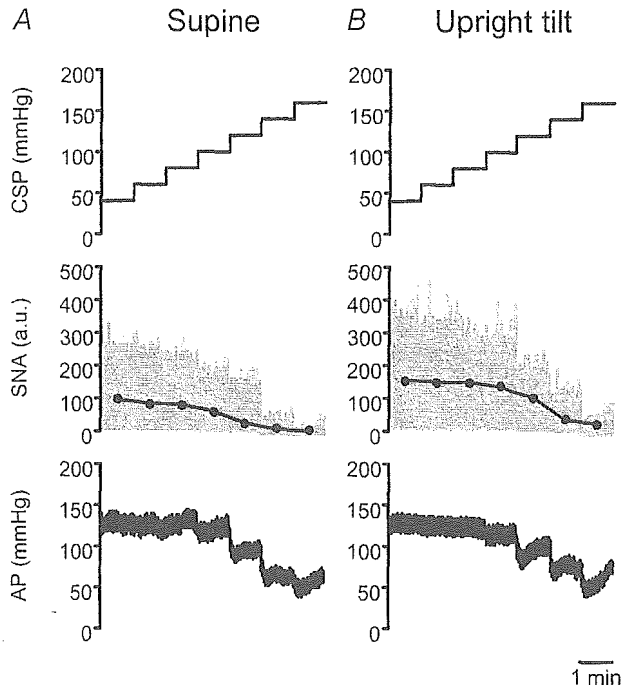

Figure 3. Time series of SNA and AP in response to stepwise increase in intracarotid sinus pressure (CSP) in supine (*A*) and 60 deg upright tilt positions (*B*)
Each CSP step was maintained for 1 min. The same animal in Fig. 2 was used in this study. Data were resampled at 10 Hz. In the middle panels, the fine vertical spikes indicate SNA signals resampled at 10 Hz, while the continuous bold line indicates data averaged over 1 min. SNA and AP decrease in response to increments in CSP for both postures. Upright tilt increases SNA at all CSP levels.

shifted the CSP–SNA curve rightward to a higher SNA. Meanwhile, in the peripheral arc, the upright tilt shifted the SNA–AP curve downward to a lower AP (Fig. 4*B*). Consequently, as the animal was changed from supine to upright tilt, the operating point estimated from the intersection of the two arcs shifted from point S to point U with a marked increase in SNA and a slight increase in AP (Fig. 4*C*). In the total arc, the upright tilt slightly steepened the CSP–AP curve, and also slightly increased the operating AP from point St to point Ut (Fig. 4*E*).

Group-averaged data show that the 60 deg upright tilt shifted the neural arc to higher SNA (Fig. 5*A*), shifted the peripheral arc to lower AP (Fig. 5*B*), and moved the operating point to markedly higher SNA (25 ± 5 a.u) while maintaining AP (Fig. 5*C*). In a simulation where 60 deg upright tilt produces no shift in the neural arc (i.e. no resetting), then the operating point during the tilt would be the intersection between the neural arc at supine and the peripheral arc at upright tilt (point A). The upright tilt would shift the operating point to a SNA (13 ± 5 a.u., Table 1) only half of that compared with when there is a neural arc shift, while the operating AP at upright tilt would decrease by 10 ± 2 mmHg.

Group-averaged data show that the 60 deg upright tilt did not change the total arc curve (Fig. 5*D*). The operating AP point in the total arc was constant during the postural change (point St overlapped with point Ut, in Fig. 5*E*). In a simulation where 60 deg upright tilt produces no shift in the neural arc (i.e. no resetting), then the tilt would shift the total arc curve downward to a lower AP (line joining crosses) and decrease the operating AP from point St to point At (Fig. 5*E*).

Group-averaged data of P_1 (the range of SNA response to CSP) and P_4 (the minimum value of SNA) in the neural arc were larger at 60 deg upright tilt than supine (Table 2). In the peripheral arc, P_1 (the range of AP response to SNA) was smaller while P_3 (midpoint of the SNA operating range) was higher at 60 deg upright tilt (Table 1). In both

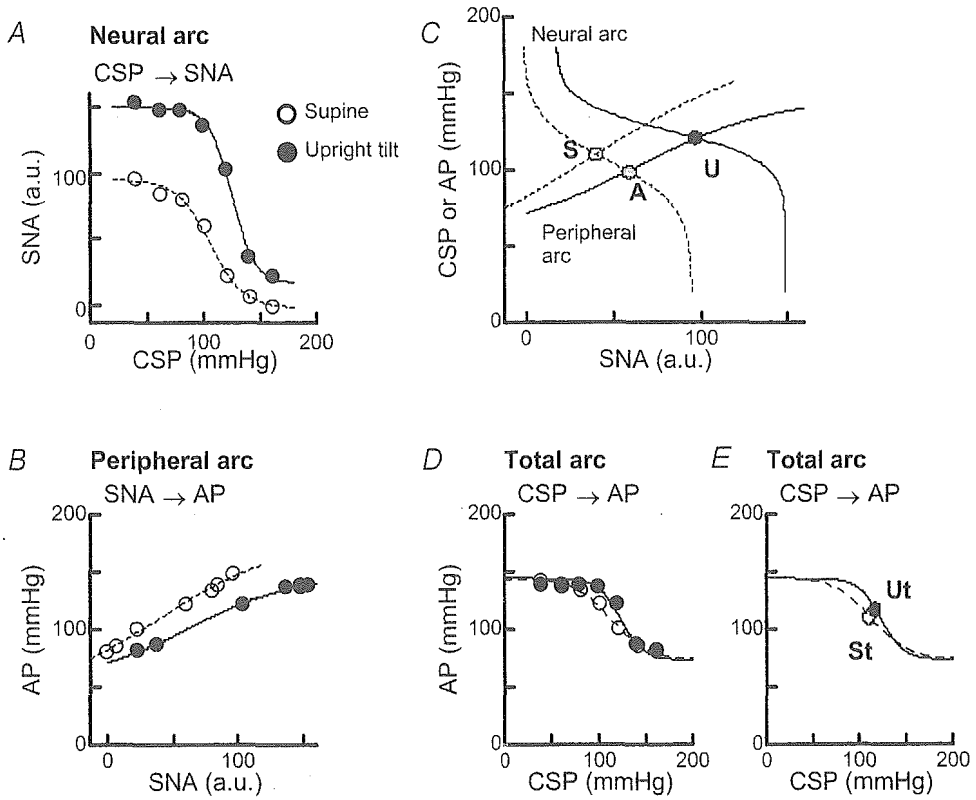

Figure 4. Example of baroreflex neural arc (*A*), peripheral arc (*B*) and total arc (*D* and *E*), and the baroreflex equilibrium diagram (*C*) in supine (○, dotted line) and 60 deg upright tilt positions (●, continuous line)

Data were obtained from the same animal as in Figs 2 and 3. The upright tilt shifts the neural arc to a higher SNA (*A*), shifts the peripheral arc to a lower AP (*B*), and moves the operating point from point S to point U (*C*). In the baroreflex equilibrium diagram (*E*), point S and U indicate the estimated operating points in supine and upright tilt positions, respectively. Point A (grey circle) indicates the estimated operating point in upright tilt position in the absence of neural arc shift (simulation) (*C*). The upright tilt slightly steepens the total arc and moves the operating AP from point St to point Ut (*D* and *E*). In the total arc (*E*), points St and Ut indicate the estimated operating points in supine and upright tilt positions, respectively.

the neural and peripheral arcs, the maximal gains (at the mid-point of the arc) and operating gains (at the intersection of arcs) were similar in supine and upright tilt positions. All parameters (P_{1-4}) and the maximal gain of the total arc were similar in supine and upright tilt positions (Table 3).

Using the data from all animals, the operating AP estimated from the baroreflex open-loop equilibrium diagram (protocols 1 and 3) agreed with those measured in the baroreflex closed-loop condition (protocol 2) for both postures (Fig. 6*A*). The operating SNA values estimated from the equilibrium diagram also agreed with those measured for both postures (Fig. 6*B*).

Discussion

The maintenance of AP in upright posture against gravitational fluid shift is of great importance, but the mechanisms remain unknown. We applied baroreflex equilibrium diagram analysis (Yamamoto *et al.* 2004) to the baroreflex system both in supine and 60 deg upright tilt positions. Our new major findings are that upright tilt shifts the CSP–SNA relationship (the baroreflex neural arc) to a higher SNA, whereas it shifts the SNA–AP relationship (the baroreflex peripheral arc) to a lower AP (Fig. 5). These data support our first hypothesis that orthostatic stress resets the baroreflex neural arc to a higher SNA.

Our data indicate that resetting of the baroreflex neural arc in an upright posture doubles the orthostatic activation of SNA and increases the operating AP by 10 mmHg. In our experiments, 60 deg upright tilt reset the neural arc to a higher SNA, shifted the peripheral arc to a lower AP (Fig. 5*A* and *B*), and consequently moved the estimated operating point from point S (SNA, 66 a.u.; AP, 102 mmHg) to point U at a higher SNA (91 a.u) and similar AP (102 mmHg) (Fig. 5*C*). In a simulation where the resetting in the neural arc is absent, 60 deg upright tilt would move the operating point from point S to point A (the intersection of the supine neural arc and the upright-tilt peripheral arc: SNA, 79 a.u.; AP, 92 mmHg),

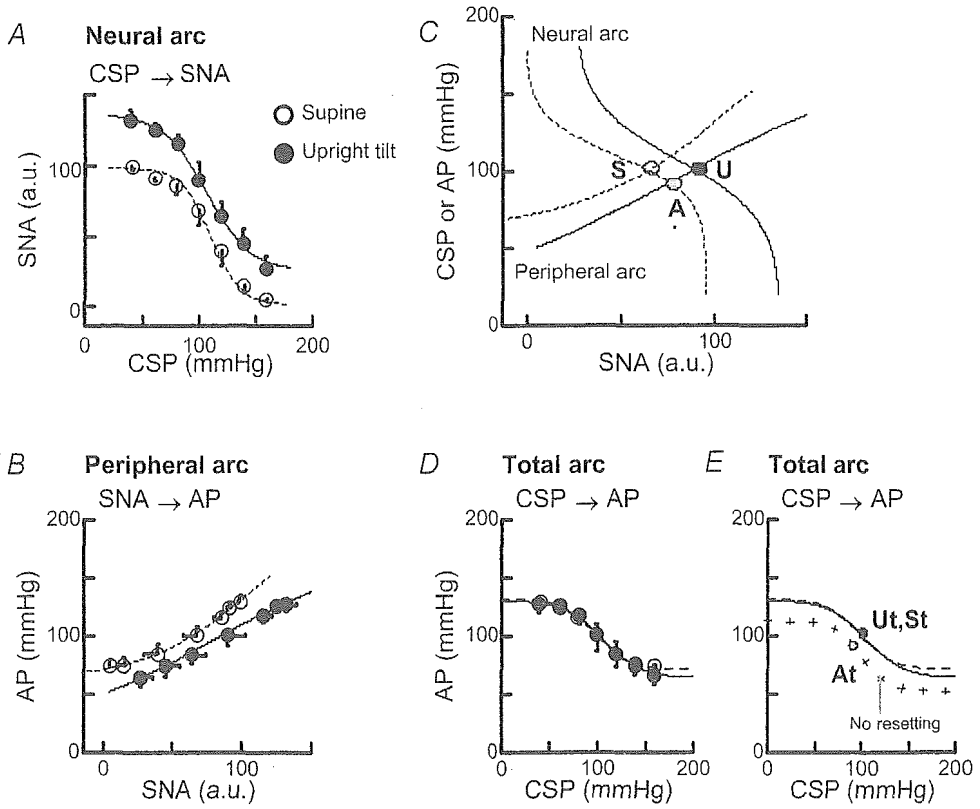

Figure 5. Baroreflex neural arc (*A*), peripheral arc (*B*) and total arc (*D* and *E*) and the baroreflex equilibrium diagram (*C*) in supine (○, dotted line) and 60 deg upright tilt positions (●, continuous line)
Data were averaged from all animals ($n = 8$) and presented as means ± S.D. Dotted and continuous lines are four-parameter logistic functions fitted to the averaged data. In the baroreflex equilibrium diagram (*C*), point S and U indicate the estimated operating points in supine and upright tilt positions, respectively. Point A (grey circle) indicates the estimated operating point in upright tilt position in the absence of neural arc shift (*C*). In the total arc (*E*), points St and Ut indicate the estimated operating points in supine and upright tilt positions, respectively. The two points are superimposed. The line joining the crosses and point At (grey circle) indicate the estimated total arc curve and operating point, respectively, in the absence of neural arc shift (simulation) (*E*).